Talanta 255 (2023) 124211

Contents lists available at ScienceDirect

Talanta

journal homepage: www.elsevier.com/locate/talanta

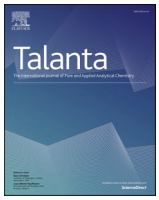

3D-printed chemiluminescence flow cells with customized cross-section geometry for enhanced analytical performance

Llucia García-Moll [a,1], Alexandra Sixto [b,1], Enrique Javier Carrasco-Correa [c,**], Manuel Miró [a,*]

[a] FI-TRACE Group, Department of Chemistry, University of the Balearic Islands, Carretera de Valldemossa km 7.5, E-07122, Palma de Mallorca, Spain
[b] Cátedra de Química Analítica, Departamento Estrella Campos, Facultad de Química, Universidad de La República, Av. Gral. Flores 2124, 11800, Montevideo, Uruguay
[c] CLECEM Group, Department of Analytical Chemistry, University of Valencia, C/ Doctor Moliner, 50, E-46100, Burjassot, Valencia, Spain

ARTICLE INFO

Handling editor: Ian D McKelvie

Keywords:
3D-printing
Flow-cell
Chemiluminescence
Flow injection
Prototyping

ABSTRACT

Low force stereolithography is exploited for the first time for one-step facile fabrication of chemiluminescence (CL) flow-through cells that bear unrivalled features as compared to those available through milling or blowing procedures or alternative 3D printing technologies. A variety of bespoke cross-section geometries with polyhedral features (namely, triangular, square, and five-side polygon) as well as semicircular cross-section are herein critically evaluated in terms of analytical performance against the standardcircular cross-section in a flat spirally-shape format. The idea behind is to maximize capture of elicited light by the new designs while leveraging 3D printing further for fabrication of (i) customized gaskets that enable reliable attaching of the active mixing zone of the CL cell to the detection window, (ii) in-line 3D-printed serpentine reactors, and (iii) flow confluences with tailorable shapes for enhancing mixing of samples with CL reagents. Up to twenty transparent functional cells were simultaneously fabricated without inner supports following post-curing and surface treatment protocols lasting less than 5 h. In fact, previous attempts to print spirally-shaped cells in one-step by resorting to less cost effective photopolymer inkjet printing technologies were unsuccessful because of the requirement of lengthy procedures (>15 days) for quantitative removal of the support material. By exploiting the phthalazinedione-hydrogen peroxide chemistry as a model reaction, the five-side irregular pentagon cell exhibited superior analytical figures of merit in terms of LOD, dynamic range and intermediate precision as compared to alternative designs. Computational fluid dynamic simulations for mapping velocities at the entry region of the spiral cell corroborated the fact that the 5-side polygon cross-section flow-cell with Y-type confluence permitted the most efficient mixing of reagents and sample while enabling larger flow velocities near the inlet that contribute to a more efficient capture of the photons from the flash-type reaction. The applicability of the 3D-printed 5-side polygon CL cell for automatic determination of hydrogen peroxide using a computerized hybrid flow system was demonstrated for the analysis of high matrix samples, viz., seawater and saliva, with relative recoveries ranging from 83 to 103%.

1. Introduction

Additive manufacturing, commonly termed 3D printing, can be categorized as an interdisciplinary technique in a wide range of fields of research, including (bio)analytical sciences [1–3]. In this context, 3D printing has opened up new avenues in the design and fast prototyping by iterative changes using computer-aided modelling of optical and electrochemical (bio)sensing platforms [2,4,5], integrated and functional microscale/flow-injection devices [6–8], porous materials for sample preparation/microextraction [7–11], and chromatographic separation phases [1,12] with dedicated functionalities. Possibilities for tailor-made fabrication of devices with intricate features using photopolymerizable or thermoplastic materials are, in principle, merely limited by our own imagination, yet most of the research to date has been geared towards printing of simple scaffolds, holders, templates or housing that are introduced in any of the steps of the analytical process including the analytical measurement/detection step [2,13]. Out of the assortment of 3D printing technologies launched to the market, fused

* Corresponding author.
** Corresponding author.
E-mail addresses: enrique.carrasco@uv.es (E.J. Carrasco-Correa), manuel.miro@uib.es (M. Miró).
[1] Both authors have equally contributed to this work.

https://doi.org/10.1016/j.talanta.2022.124211
Received 1 November 2022; Received in revised form 18 December 2022; Accepted 20 December 2022
Available online 24 December 2022

deposition modelling (FDM) using affordable consumer-grade printers has attracted a great deal of attention for production of one-step bespoke prints that are adaptable to analytical detection systems [14]. Interesting examples are found in recent literature reporting the fabrication of customizable and versatile electrochemical cells and electrodes using conductive filaments [15] along with scaffolds and detection cells with adjustable optical length [16], and customized arrangements for optical detection to which light emitting diodes, photodiodes and/or optical fibers are readily integrated [17]. An additional advantage of multi-material FDM printers is the possibility of simultaneous usage of filament materials with distinct optical transparency features that demonstrated utility for minimization of stray light in photometric cells [18]. However, the limited chemical compatibility of commonly used thermoplastics (e.g., polylactic acid) [16], and the inability to withstand moderate flow pressures [17] make the actual applicability of FDM for printing of flow-through detection platforms debatable. The improved chemical and flow resistance (water tight prints) of alternative additive manufacturing technologies (*viz.*, vat polymerization (also called stereolithography, SL) or photopolymer inkjet printing (PIP)) that enable (i) higher throughput for fabrication of multiple devices, (ii) minimal feature sizes (layer thickness) and (iii) improved quality surface finishes against FDM can be fully leveraged for expanding the applicability of 3D printing to fabricate detection components in flow injection setups [13]. In both techniques, a light source selectively cures a photopolymer liquid resin on a moving platform by using (i) UV-curing lamp (PIP), (ii) laser beam (low force stereolithography, LFS) or (iii) LED in the absence of masks (digital light processing, DLP) [19]. Notwithstanding the advantageous features of LFS/DLP and PIP for potential fabrication of functional devices with entirely new formats, little effort has been dedicated to build flow-cells and functional components of luminescence detection systems, in particular, for chemiluminescence (CL) detection. Standard quartz flow cells are of rigid architecture, with pre-defined inner volume and dimensions so that redesign by glass blowing needs specialist infrastructure [20,21]. Polymeric tubing for assembling flat flow-cells is also limited by available inner diameter (ID) dimensions, and the reproducible mounting of the coiled tubing onto the photodetector might be a daunting task [22]. To shed light on the opportunities of 3D printing in the CL detection field, the seminal work by Francis' group [23] in which bespoke 3D-printed PIP flow-cells were critically compared against CNC milled counterparts for ameliorating mixing efficiency and light capture from permanganate chemistry-based reactions is worth mentioning. Unfortunately, the authors did not succeed in fabricating closed channels for the CL printed cells because of technical issues for quantitative removal/melting of the support wax inside the channels even after heating at 70 °C and sonication at high temperature. Hence, they opted for a multi-stage fabrication process of open spiral channel, thus resembling the steps of milling schemes, with further sealing by application of a transparent epoxy-acetate film operating as a window. Mounting of the printed CL onto the photodetector was also not straightforward and a purpose-build aluminium holder incorporating a reflective element was needed for comparable performance with that of milled cells [23]. Further studies by Gupta et al. [24] in which the wax was replaced by a water-soluble support material revealed that post-PIP processing of closed spiral cells with soaking in alkaline solution and intermittent sonication required more than 15 days for complete clearance of the support. This lengthy rinsing procedure corroborated the unsuitability of PIP printing for 3D fabrication of analytical flow-cells with tortuous structure. In addition, the high start-up expenses of PIP printing negate its actual applicability for affordable and fast prototyping of analytical devices.

In this work, we demonstrated for the first time the unique opportunities of LFS for one-step simple fabrication of flow-through CL cells bearing tortuous spirally-shaped geometry, with rapid post-LFS processing in a few hours. To simplify the assembly of the detection components, a rugged press-fit mounting of the bespoke 3D-printed cell onto the active area of the photodetector is ensured by a printed ring-shaped housing. More sophisticated 3D channel designs encompassing unrivalled cross-section geometries that are inaccessible by CNC milling processes and diverge from the traditional circular cross-sections of standard flow-cells are also to be herein evaluated in terms of analytical performance using the phthalazinedione chemistry for determination of reactive oxygen species as a proof of concept applicability. The idea behind is to assess the effect of several polyhedral shapes (namely, triangular, square, and five-side polygon) as well as semicircular shapes of CL cell channels and distinct formats of fluidic confluences for efficient mixing and capture of elicited light in the vicinity of the detection system. To this end, a simple and fully automatic two-syringe flow arrangement was assembled for rapid mixing of reactants and analyte aiming at detection of hydrogen peroxide in biological and marine samples at concentration levels significantly lower than those reported using alternative radial-shaped 3D-printed flow cells [24].

2. Experimental

2.1. Reagents and solutions

All the chemicals, unless otherwise stated, were of analytical reagent grade. Solutions were prepared using Milli-Q water (Merck-Millipore, Darmstadt Germany) with a resistivity ≥18.2 MΩ·cm. The chemiluminogenic reagent consisted of 0.5 mmol/L 3-aminophthalhydrazide (luminol) (Sigma-Aldrich/Merck KGaA, Darmstadt, Germany) dissolved in 1 mol/L NH_4OH (Fisher Scientific SL, Madrid, Spain) and 0.1 mol/L K_2CO_3 (Fisher Scientific). The reagent was let stand for at least three days at 4 °C in the dark pending use followed by pH adjustment to 10.8 with concentrated HCl (Fisher Scientific). A 0.25 mmol/L Co(II), used as a catalyser, was prepared from $Co(NO_3)_2{\cdot}6H_2O$ (Fisher Scientific).

An intermediate standard solution of 0.1 mol/L H_2O_2 (Sigma-Aldrich/Merck KGaA) was titrated against 0.2 mol/L $KMNO_4$ (Fisher Scientific) twice a week and working standard solutions were prepared just before analysis. The permanganate reagent was titrated weekly against sodium oxalate (Fisher Scientific). Working standard solutions of H_2O_2 were prepared by serial dilution of the stock within the concentration range spanning from 50 nmol/L to 1000 nmol/L.

Fluidic platforms (flow-through cells and mixing coil) were 3D-printed by resorting to the FLGPCL02 (Formlabs, Barcelona, Spain) clear resin. Isopropyl alcohol (IPA, Fisher Scientific) was used for removal of the resin residues within the channels of the 3D-printed devices.

Seawater surrogate was prepared according to Weztel and Likens' recommendations [25] by dissolving the following salts and chemicals in Milli-Q water: 3.0 mg L^{-1} NaF, 20 mg L^{-1} $SrCl_2{\cdot}6H_2O$, 30 mg L^{-1} H_3BO_3, 100 mg L^{-1} KBr, 700 mg L^{-1} KCl, 1470 mg L^{-1} $CaCl_2{\cdot}2H_2O$, 4000 mg L^{-1} Na_2SO_4, 10,780 mg L^{-1} $MgCl_2{\cdot}6H_2O$, 23,500 mg L^{-1} NaCl, 20 mg L^{-1} $Na_2SiO_3{\cdot}9H_2O$, and 200 mg L^{-1} $NaHCO_3$, all of them from Fisher Scientific SL. Human saliva matrix (5 mL) was collected from a healthy volunteer aged >18 yr by spitting in a polypropylene tube just before analysis, filtrated through a 0.45 μm nylon filter, and diluted 1:1000 previous hydrogen peroxide determination. The participant provided informed consent before participating in this project that was approved by the Research Ethics Committee of the Balearic Islands (ID no. IB 3776/18 PI).

2.2. Fabrication of the 3D-printed devices

The LFS fluidic devices (CL flow-through cell and mixing coil) were modelled via the freeware FreeCAD software (www.freecadweb.org). Five flow-through spirally-shaped cells with different cross-sectional channel geometry were designed and one-step printed (see Fig. 1): circular, semicircular, triangular, square and 5-side polygon (irregular pentagon). The overall cells were fabricated in cylindrical-shaped modules with an outer diameter of 25 mm and height of 21 mm. Notwithstanding the distinct geometrical features, all cells bear a

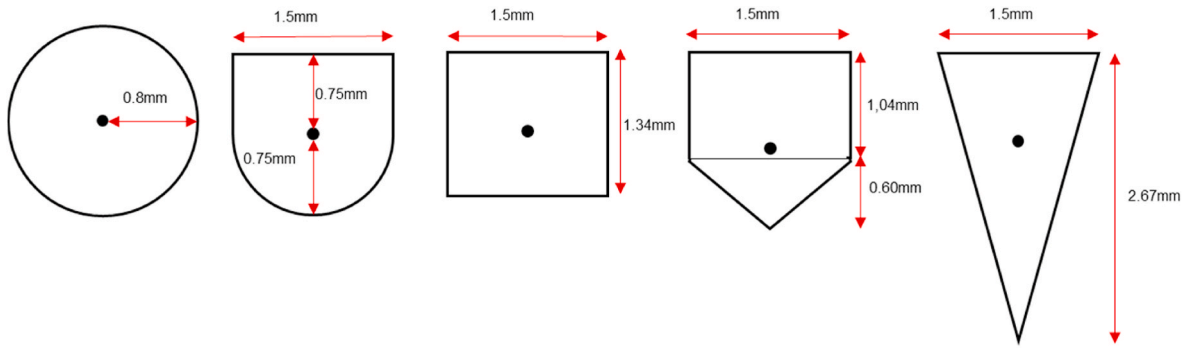

Fig. 1. Nominal dimensions of the different cross-sectional geometries of the spirally-shaped 3D-printed CL flow cells.

nominal length of 110 mm and a nominal total volume of 221 μL, which is one order of magnitude larger than that of previous 3D-printed cells using PIP printing [24]. The enclosed channel geometries were devised aimed at maximizing the volume of reactant zones in close contact with the detector window for efficient capture of light from the flash CL reaction. Thus, the polyhedral base of the semicircular, triangular, square or 5-side polygon channels, all 1.5 mm wide, was attached to the photomultiplier (PMT) window (see Fig. 1). The standard cylindrical cell was fabricated with 1.6 mm ID so as to bear identical inner volume than that of the rest of designs, and served as a reference for evaluating the performance of the novel channel configurations.

The spirally-shaped flat flow-cells ended on one side with an integrated T-shaped upright connector of 1.5 mm ID to mix the reagents (luminol and Co(II)) with the sample at straight angle (Fig. S1A). Two inlets of 5.5 mm ID and 8 mm length each were printed on top of the connector for tapered thread coupling of the CL cell with the flow system using nuts and flangeless tubing (Fig. 2A and B). Alternative Y-shaped and Y′-shaped connectors were also evaluated for the sake of improving mixing (Figs. S1B and S1C). Both configurations were modelled to have protruding channels of 1.5 mm ID and identical inlets than those of the T-shaped counterpart. The main difference relies on the angles connecting the inlets with the outlet conduit, namely 135° angle tilt relative to the outlet (Figs. S1B and S1C). The other end of the spirally shaped cell consists of an upright outlet of 5.5 mm ID for tapered thread connection to waste (see Fig. 2A).

The flexibility of 3D printing was leveraged for fabrication of 3D serpentine coils for proper mixing of the reagents (luminol and Co(II)) prior to downstream merging the sample (Fig. 2C). The overall size of the unit was 15 mm high, 15 mm wide and 29 mm long with an inner volume of ca. 160 μL. The coil was designed to have a 50 mm effective length with a 2 mm ID conduit and turnings of 5.3 mm diameter that were 3 mm distant each other. Further, a cylindrical ring (47 mm OD and 26 mm ID) was printed for reliable mounting of the flow-cell face-to-face to the PMT by press-fitting.

The STL files of the bespoke 3D platforms were loaded in the manufacturer's software (Preform, Formlabs) for slicing and orientation prior to 3D printing via the LFS Form 3 printer (Formlabs, Somerville, MA, USA). The devices were printed at a nominal resolution of 50 μm (440 layers as a trade-off between speed and resolution of the final print) using the FLGPCL02 (Formlabs) clear resin. All devices were printed with the spirally shaped channel face downward using 3 mm-high outer supports onto the confluence face to facilitate their removal from the build platform without jeopardising the surface properties (e.g., smoothness and transparency) of the face to be coupled to the PMT.

After retrieving the 3D-printed devices from the printer, the "green" objects were post-processed by a multi-step operational procedure. Briefly, the devices were soaked in isopropyl alcohol (IPA) for 10 min in an ultrasonic bath to remove the non-polymerized resin. Then, the closed channels were manually perfused with *ca.* 50 mL IPA to eliminate remnants of liquid resin. Afterwards, the prints were soaked in water for 10 min in an ultrasonic bath, followed by a third ultrasonic-based cleaning procedure, now in IPA. Finally, the 3D-printed devices were dried with nitrogen and UV-postcured for 1 h under a 16 W low pressure mercury lamp UV oven (KA-9180, PSKY, China) to harden the polymerized resin and prevent unspecific leaching of non-polymerized oligomers. Once the post-printing process was finished, the two inlets and outlet of the CL cells were manually tapered to 1⁄4" - 28 threads. The 3D flow-cells were finally sanded consecutively with 1000 and 3000 grain sandpaper on the spiral channel face in order to improve their transparency for CL measurements and fit it tightly to the PMT. To make the flow-cell even more transparent, a minute amount of clear resin was manually applied after sanding to the external face, homogenized by rubbing and finally post-cured *ca.* 3 h under 16 W UV light.

To study the inner channel structure and the possible reactivity of the printed devices, several optical characterization studies were carried out by scanning electron microscopy (HITACHI S–3400 N, Ibaraki, Japan) and attenuated total reflection-infrared spectroscopy (Bruker, Germany).

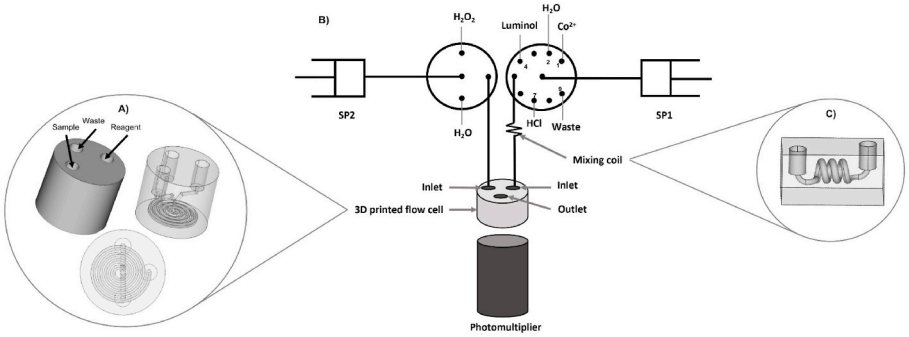

Fig. 2. Schematic illustration of the flow manifold assembled for investigation of the analytical features of 3D-printed flow-cells with distinct cross-sectional geometries for the chemiluminescence detection of hydrogen peroxide: A) Spirally-shaped flow-cell design, B) Flow manifold and C) Serpentine mixing coil.

2.3. Flow manifold and chemiluminescence detection

A diagrammatic representation of the flow manifold for evaluation of the 3D-printed flow-cells aimed at the CL detection of hydrogen peroxide is presented in Fig. 2. The system is composed of two automatic bi-directional syringe pumps (SP, Cavro, Tecan, Sunnyvale, USA) equipped with gas-tight glass syringes (Hamilton, Bonaduz, Switzerland). One pump, used for the samples or standards (SP2), was fitted with a 1 mL glass syringe and a three-way valve (VICI AG International, Schenkon, Switzerland) on its head, which allowed connection with the flow manifold or the solutions to be analyzed. The other pump (SP1) furnished with a 5 mL glass syringe and a 9-port selection valve (VICI AG International) on its top, was used for in-situ mixing the two CL reagents (luminol and Co(II)) in-syringe. The reagent mixture was herein employed as a carrier solution. All the connections were made from 0.8 mm i.d. fluorinated ethylene-propylene (FEP) tubing. The 3D-printed serpentine mixing coil (see Fig. 2) was connected between the 9-port selection valve of SP1 and the flow-through cell for further improvement of the mixing of reagents.

A photomultiplier H9319 (Hamamatsu, Shizuoka, Japan) with an optical window of 22 mm was selected as a photodetector. The 3D-printed spirally-shaped flow-cell mounted over the detector window and integrating a flow confluence (see Fig. 2) permitted reagents and sample to be mixed directly in front of the photomultiplier tube (PMT). The overall CL detection components were arranged in a light-tight home-made box.

CocoSoft 5.16 software package written in Phyton [26] is utilized in this work for fully automatic metering of the sample/reagent volumes, and controlling of the position of the multi-position and three-way valves, speed of the SP, and acquisition of CL data. The CL peak height integrated by Chromophoreasy.xlsm [27] was used as the analytical signal throughout.

2.4. Flow-based analytical procedure

Prior to use for the first time, the flow-through cell was flushed with luminol/Co(II)/700 nM H_2O_2 and filled with CL reagent overnight for further leaching of non-polymerized oligomers and cross-linking agents (urethane and acrylate moieties) under alkaline conditions while serving for cell ageing/passivation to obtain low baseline CL levels and repeatable analyte readouts afterwards.

The automatic flow method starts by filling the reagent channels with 250 μL of luminol (from port 4, see Fig. 2) and 200 μL of Co(II) (from port 1) through the 9-position head valve from SP1, and 200 μL of sample or standard solution through the three-way valve from SP2, which are whereupon directed to waste. Then, SP1 is rinsed with 500 μL of luminol at 2000 μL min^{-1}. Afterwards, SP2 is set to aspirate 380 μL of sample/standard from which 80 μL were dispensed towards the manifold to fill the communication line between SP2 and the flow-through cell. Afterwards, SP1 is programmed to aspirate five segments of 960 μL of luminol at 5000 μL min^{-1} that are interdispersed in-syringe in tandem with four 50 μL segments of Co(II) aspirated at 2000 μL min^{-1}. Then, 700 μL of the *in-situ* mixed Co(II)-luminol reagent is dispensed forward through the 3D-printed flow-through mixing reactor at 1000 μL min^{-1} towards the 3D-printed flow-cell for recording of the background CL signal. At this moment, data acquisition is automatically initiated and is followed by performing six replicate injections of 50 μL of sample or standard every 23 s at 1500 μL min^{-1} into a continuously flowing reagent stream of luminol-Co(II) composite reagent at 1000 μL min^{-1}. In the case of the T-confluence and because of unwanted dispersion of the reagent flowing stream into the sample, while keeping it stagnant, prior to inject the next sample plug, a burst of 10 μL of sample is pumped forward to rinse the sample channel, and thus fresh sample is available to react with the CL reagent. To minimize analyte carryover, SP1 was rinsed with 1 mL of Milli-Q water at 2500 μL min^{-1} prior to analysing the ensuing standard or sample. At the end of the working day, the manifold was cleaned with 5 mL of 0.5 mol/L HCl followed by flushing with 10 mL of Milli-Q water at 5000 μL min^{-1}.

2.5. Computational fluid dynamics

The investigation of the fluid dynamics of the reagent and the sample zones at the confluence point towards the inlet of the distinct spirally-shaped CL cells was performed using the freeware Simscale (www.simscale.com). The simulations were undertaken at the time that the standard or sample is injected along with the mixed reagent in the flow system at the flow-rates indicated above using water as the solvent in all cases. The fluid dynamics were estimated based on the k-omega SST model, the steady-state time dependency and the SIMPLE algorithm options using incompressible analysis. Color mapping near the inlet of the spirally shaped cells that stands for distinct ranges of flow rates was provided by Simscale.

3. Results and discussion

3.1. Physicochemical characterization of the 3D-printed flow-cells

The actual channel cross-section features of the 3D-printed spiral flow-cells as obtained by LFS using the consumer-grade Form 3 printer were evaluated by SEM. To this end, short open-ended channels with the distinct five geometries (circular, semicircular, triangular, square and 5-side polygon) were 3D-printed and characterized. As shown in Fig. 3, the SEM images enable elucidating the printing accuracy of the various CAD cross-section geometries for the spirally-shaped channels.

Table 1 compiles the real volume of the different flow-cells, estimated from the actual features of the SEM micrographs, and the printing precision of several prints (n = 3) of every flow-cell as compared to the nominal volume (221 μL). As can be seen in Table 1, the volume difference % is, in general, acceptable for practically all of the flow-cell geometries (<4.1%), except for the triangular shape geometry with deviations as high as 25%. This observation is attributed to the limited resolution of the LFS printer at the vertex of the triangle legs that causes resin crosspolymerization with the consequent deviation from the triangular expected shape of the structure. It should be noted that the low volume difference of the square shape is most likely a consequence of the fact that point-by-point polymerization is more reliable for polyhedral features with rectangular angles. Acceptable intermediate precision was found for all the geometries, yet higher values were found for the triangular cross-section (7.2% RSD) because of technical issues for reliable fabrication of triangular shapes in non-supported 3D-printed structures.

One of the potential problems related with 3D printing in milli/microfluidic platforms refers to the surface chemical changes that the 3D-printed photopolymer might undergo due to the intermittent/continuous pumping of reagents and samples. Therefore, it is important to evaluate the stability and the potential chemical modification of the surfaces of the closed channels of the 3D-printed platforms by the chemicals that will be used in the ensuing CL reactions (see SI for details and Table S1). Our experimental findings however revealed that the surface groups of the printed resin were not changed for any of the tested solutions in this work as appreciated by FT-IR attenuated total reflectance spectroscopy (see Fig. S2). Therefore, the immobilization of the CL reagents or reactivity with the post-processed 3D-printed cells is proven negligible.

The optical properties and chemical resistance of 3D-printed LFS platforms using Clean resin have been extensively studied elsewhere [28]. Transmittance readouts indicated poor optical transparency at the UV region and the higher end of the visible spectrum, yet with a sharp increase from 420 nm and onwards, thus permitting applicability for light capture at the highest emission wavelength of the luminol–H_2O_2–Co(II) CL system, that is, 430 nm.

An important parameter to study in the development of novel flow-

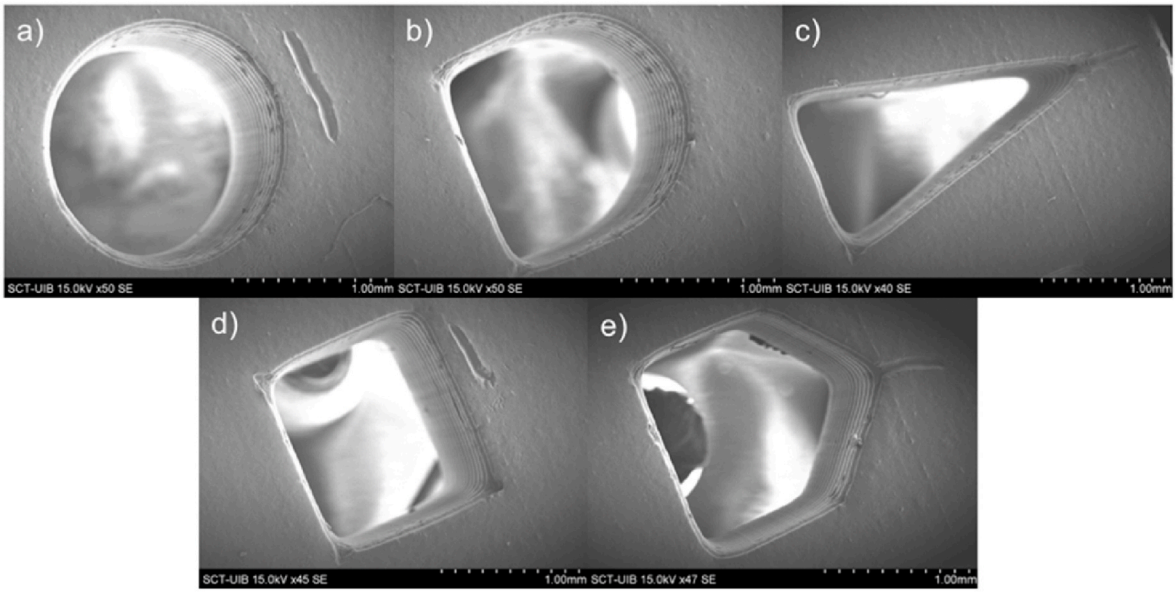

Fig. 3. SEM micrographs of the circular (a), semicircular (b), triangular (c), square (d) and 5-side polygon (e) geometries of the spirally-shaped channels of the 3D printed flow-cells.

Table 1
Estimation of the volume of the 3D-printed flow-cells using the SEM micrographs as compared to nominal values.

Flow-cell geometry	Theoretical Volume (mm^3)	Estimated Volume (mm^3)/RSD (%)	Volume difference (%)
Circular	221	227 ± 4/1.8	2.7
Semicircular	221	230 ± 2/0.9	4.1
Triangular	221	166 ± 12/7.2	−25.0
Square	221	223 ± 8/3.6	0.9
5-side polygon	221	213 ± 11/5.2	−3.6

cells for flash CL reactions is the actual volume of chemiluminogenic reagents/sample mixture that is exposed to the detector window. A large volume of liquid in the vicinity of the PTM enables collecting a greater amount of elicited light while minimizing autoabsorption phenomena that might be particularly relevant in biological samples. In our work, the accumulated liquid volume in increasing longitudinal sections (250 μm long each) from the detector window was calculated for each of the printed cells using the geometrical dimensions estimated by SEM (See Fig. 4). The circular and triangular cross-section shapes are those with the lowest accumulated liquid volume within the first 500 μm (*ca.* 60 and 64 mm^3, respectively) compared to the semicircular, square and 5-side polygon cross-section features (*ca.* 82, 84 and 82 mm^3, respectively) corresponding to *ca.* 30% volume difference. The entirely available volume for all cross-section geometries was found at ca. 1.5 mm vertical distance from PTM expect for the triangular shape that is more than 2.25 mm long. It is important to note that the ratio of the volume within the first 250 μm (V_i) to the total cell volume (V_t) (see Fig. 4) is distinguishably lower (ca. 10%) for the standard cylindrical cell as compared to the rest of designs (ca. 20%), thereby indicating that the new printed configurations might provide superior performance for flash CL reactions. Another interesting observation is that the cross-section geometries that feature *ca.* 80% of the total available volume at shorter

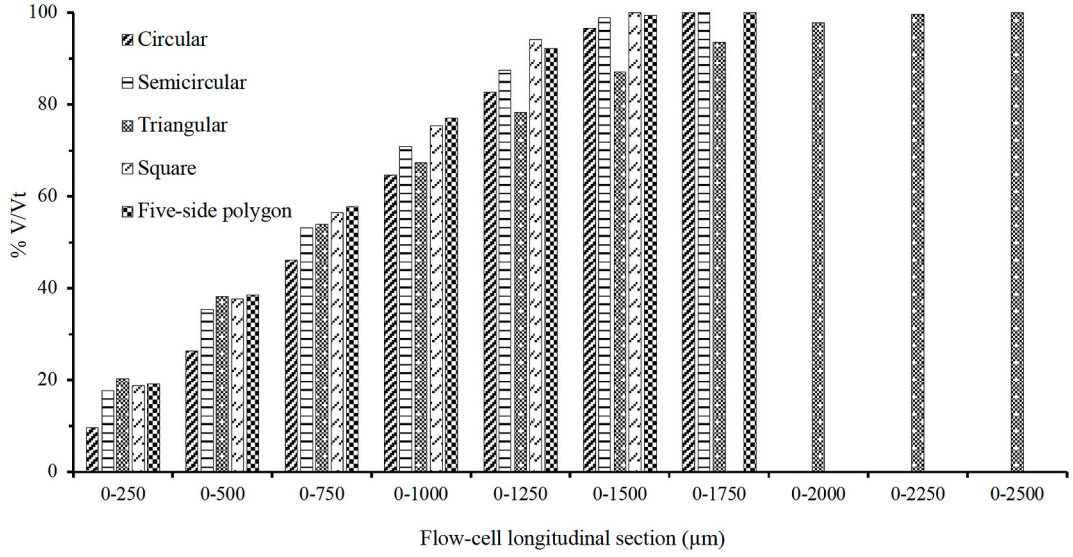

Fig. 4. Relative accumulated volume (%) of the different flow-cells at varied longitudinal sections from the detector window as calculated from the experimental geometrical features obtained by SEM (Fig. 2).

distances (1.0 mm) are the square and the pentagonal shapes corresponding to ca. 168 and 165 mm^3, respectively (Fig. 4), and thus they are the most appealing configurations for efficient capture of the elicited light.

3.2. Characterization of the flow-through CL system

Preliminary studies were undertaken using the 3D-printed flow-cell with circular cross-section for characterization of the configuration of the hybrid flow system. A T-shaped connector (180°, see Fig. S1A) was modelled in the body of the 3D-printed structure to merge the reagent and sample downstream just before entering into the spiral channel. The proposed flow system capitalizes upon discontinuous/pulse sample injection and therefore enables low consumption of sample compared to the conventional FI systems [29–31], which is particularly needed in biological assays (*e.g.* saliva). The use of two stand-alone syringes enables greater versatility in changing volumes and flow-rates with respect to FI manifolds or multisyringe flow injection counterparts [32] in which several syringes operate concomitantly. Chemical parameters (pH, and blank signal minimization) and hydrodynamic parameters (injection volume, flow-rate, and mixture of reagents) were investigated with the automatic flow system aimed at maximizing the CL signal intensity.

The pH of the CL reagent is a pivotal parameter for proper Co(II)-catalyzed luminol oxidation by H_2O_2. Based on literature data, a pH ranging from 10 to 11, namely 10.8 was selected [30,33]. The off-line/on-line preparation of composite reagent (luminol + Co(II)) might significantly influence the intensity of elicited CL light under flowing stream conditions. The use of a previously mixed reagent solution [30,34] was discarded because cobalt hydroxide rather than Co(II) is the thermodynamically stable species at pH 10.8 according to the Pourbaix diagram of the cobalt-water system. Instead, in-situ automatic mixing of the two reagents was performed in-syringe. For this purpose, five segments of 960 μL of luminol were aspirated in tandem with four 50 μL segments of Co(II), and further mixed backward within the 3D-printed serpentine reactor toward the flow-cell. Because of the flash characteristics of the CL reaction selected as a model reaction, high flow-rates for mixing sample and reagents are necessary, yet limitation is here given by the stability of the flow-cell and connections under moderately high flow pressures. In line with previous studies [24,30], the flow-rate was set to 1000 μL min^{-1} for the CL composite reagent (serving as a carrier stream) and 1500 μL min^{-1} for injection of the standards and samples.

Initial tests indicated that the reliability of the flow-through CL method was jeopardized by high and unrepeatable blank signals that are attributed to the generation of reactive oxygen species (ROS) by the photolysis of potential organic components of the distilled/reverse osmosis water feeding the Milli-Q water fabrication system, as reported by other authors [34,35]. Note that ROS traces in the catalyst or chemiluminogenic reagent will merely consume minute amounts of luminol, yet no blank contribution in the CL flow system is expected because the flash CL reaction of contaminant-laden water with luminol will occur in-syringe. The contamination of Milli-Q water with traces of ROS was corroborated by performing increasing volume injections of blank (50, 75, 100 and 125 μL). A linear trend of the peak height *versus* the injection volume was encountered. Removal of trace amounts of H_2O_2 from water by use of a manganese oxide microcolumn [33,36], catalase treatment at appropriate pH [37] or filtration and storage in the dark for at least 2 weeks [30] were reported in the literature. In this work, the latter was selected for the Milli-Q water treatment prior to prepare the blank/standard solutions, the CL reagent, the synthetic seawater and the diluted saliva.

The sample injection volume was optimized based on the largest possible amount that could be efficiently mixed with the reagent in the way towards the detector. Hence, injection volumes ranging from 25 to 100 μL of sample were evaluated. The appearance of a non-Gaussian peak was clearly observed for volumes greater than 50 μL. This was attributed to the fact that the internal channels of the 3D-printed flow-cells as obtained by LFS are characterized by surface roughness, thereby altering flow hydrodynamics and decreasing dispersion of reagents and sample within the short conduit communicating the confluence point with the inlet of the flow-cell. This observation is however positive to prevent triggering the flash CL reaction prior reaching the detection zone. The injection volume was finally set to 50 μL for the ensuing experiments.

3.3. Analytical performance and fluid dynamic simulations

The analytical performance of the flowing stream CL methods incorporating 3D-printed flow-cells with distinct cross-sectional geometry was evaluated in terms of intermediate precision (intra-day and cell-to-cell reproducibility), limit of detection (LOD) based on the $3S_{blank}$ criterion, and sensitivity following IUPAC recommendations (see Table 2). Calibration graphs were constructed using eight different H_2O_2 standard concentrations ranging from 50 nM to 1000 nM. The analytical blank was determined using Milli-Q water, which was analyzed in the same way than the standards and includes any signal contribution associated with the solvent itself (see Experimental). Under the selected experimental conditions, a log-log linear graph typically described in CL assays [32,34,38] of light emission *versus* hydrogen peroxide concentration was found over the range previously mentioned for every individual flow-cell. As can be seen in Table 2, linear relationships were found ($R^2 > 0.993$) for all the geometries.

The intermediate precision of the CL methods was evaluated using the relative standard deviation (% RSD) of the intra-day (n = 6) and cell-to-cell (n = 3) data for the overall 3D-printed designs at the 100 nM and 500 nM levels. A schematic illustration of the fiagram obtained in repeatability studies is shown in Fig. S3. The best intra-day RSD values using the T-confluence were found for the square (1.7%), 5-side polygon (2.6%) and the conventional circular cross-section (2.1%) geometries at the 100 nM level. Again, cell-to-cell precision that relies on the geometry–dependent printer reliability and resolution indicates superior performance of the square (5.7%), 5-side polygon (5.6%) and the circular (3.4%) counterpart, yet the triangular cell RSD increased up to 9.4%. The elevated cell-to-cell RSD of the triangular shape is the result of technical issues for reliable point-by-point LFS polymerization of the internal channel without inner support material.

Table 2
Analytical figures of merit of flow-through CL methods incorporating 3D printed cells for determination of hydrogen peroxide as a model analyte.

Flow-cell	Precision at the 100 nM level (%)		LOD (nM)	Sensitivity /t_{exp}	R^2 (50-1000 nM)
	Intra-day	Cell-to-cell			
Circular **(T-shaped)**	2.1	3.4	49	1.01 ± 0.02/-	0.997
Semicircular **(T-shaped)**	4.1	6.2	54	1.37 ± 0.06/ 2.97[a]	0.993
Triangular **(T-shaped)**	7.8	9.4	49	1.13 ± 0.04/ 1.26[a]	0.997
Square **(T-shaped)**	1.7	5.7	39	1.38 ± 0.04/ 3.69[a]	0.998
5-side polygon **(T-shaped)**	2.6	5.6	21	1.39 ± 0.03/ 4.08[a]	0.999
5-side polygon **(Y-shaped)**	1.0	4.8	12	1.44 ± 0.06/ 0.81[b]	0.995
5-side polygon **(Y′-shaped)**	3.9	12.9	48	1.19 ± 0.06/ 2.01[b]	0.995

[a] Comparing the sensitivity versus that of the circular (T-shaped) flow-cell at α=0,05 for 8 degrees of freedom [39]. $t_{crit} = 2.31$.

[b] Comparing the sensitivity versus that of the 5-side polygon (T-shaped) flow-cell at ∝=0.05 for 6 degrees of freedom [39]. $t_{crit} = 2.45$.

The LODs of methods incorporating the various CL cells with 3D-printed T-shaped connectors are similar (see Table 2), within the range of 39–54 nM, except for the 5-side polygon cross-section flow-cell, which features the lowest LOD value (21 nM). In fact, the LOD of the latter is 57% lower than that of the circular cross-section flow-cell. For the sake of comparison, a milled flat spiral cylindrical cell (80 μL, 1.0 mm i.d., and 14 mm observation window) made of polymetylmethacrylate (PMMA) and sealed with a window of the same material, which was adapted from previous flow systems capitalized on the luminol chemistry [40], was assembled in our manifold. Experimental results obtained under the selected experimental conditions revealed that twice as high CL readouts at the 100 nM H_2O_2 level were obtained for the 3D-printed cell with 5-side polygon cross-section with twice as low LOD and significantly better repeatability at the 100 nM as compared to the PMMA cell (2.6% vs 5.4%, respectively).

Comparing the CL method sensitivity using the standard cylindrical flow-cell with that of the new four printed designs, statistically higher values were obtained for the semicircular, square and 5-side polygon cross-sections (see Table 2). This behavior can be explained on the basis of the available liquid volume in the vicinity of the detector window. The larger the absolute liquid volume contained in the flow-cell longitudinal section from 0 to 500 μm, the greater is the CL method sensitivity. In fact, a lineal relationship (see Fig. S4) was encountered between the estimated liquid volume within the 0–500 μm against the slope of the calibration curves ($R^2 = 0.980$).

To understand the impact of the distinct geometries on the analytical performance, the fluid dynamics at the entry of the flow-cells for the concomitant pumping of the composite reagent and sample should be investigated. Computer fluid dynamics (CFD) will shed light into the effect of the cross-sectional geometry on the changes of liquid velocity *vs* position after the mixing of the reagent and sample plugs by plotting flow fields (see Fig. 5A–E). According to the CFD results, the triangular structure (Fig. 5C) showed the largest percentage of low flow-rate regions (blue and green zones under 2.1 mL min^{-1}, *ca.* 65%) as compared with the nominal flow rate (2.5 mL min^{-1}). On the other hand, the 5-side prolygon cross-section flow-cell (Fig. 5E) showcases the largest velocities with the minimum percentage of green and blue zones (*ca.* 15%), followed by the square, semicircular and circular cross-section flow-cells (*ca.* 25% of low flow-rate regions). This is in good agreement with the sensitivity and LOD data reported in Table 2, because the greater the flow-rate at the inlet of the spirally-shaped cell and within the detection zone for CL flash reactions the larger is the amount of elicited light efficiently captured by the PTM. Therefore, the 5-side polygon cross-section geometry was selected for further studies on account of featuring the lowest LOD values and improved sensitivity against those of the cylindrical geometry.

The effect of the confluence type upon mixing of reagents and sample towards the flow-cell was further explored. In this sense, 3D-printed Y and Y′-type confluence arrangements (right angle between inlets and 135° or 90° between inlets and outlet, see Figs. S1B and S5B, and Figs. S1C and S5C, respectively) were compared against the previously used T-shape connector (Figs. S1A and S5A). The intra-day repeatability (% RSD) (n = 6) and the cell-to-cell precision (n = 3) of the CL methods were quite similar for the T and Y shapes, which feature satisfactory RSD values (2.6 and 5.6% for the T-confluence, and 1.0 and 4.8% for the Y-confluence, respectively, see Table 2). On the other hand, the intra-day and cell-to-cell RSDs of the Y′-type cell, because of technical difficulties for repeatable printing of the conduit intersection, increased up to 3.9% and 12.9%, respectively. Regarding LODs of the different flow confluences (T, Y and Y′), twice as much better LOD was achieved with the Y-confluence (*viz.*, 12 nM). The CFD simulation demonstrates that the Y-type connector eliminates the dispersion of the reagent flow into the sample conduit (Fig. S5B) as opposed to the T arrangement (Fig. S5A), and thus, the injection of prior 10 μL-sample into the reagent stream as

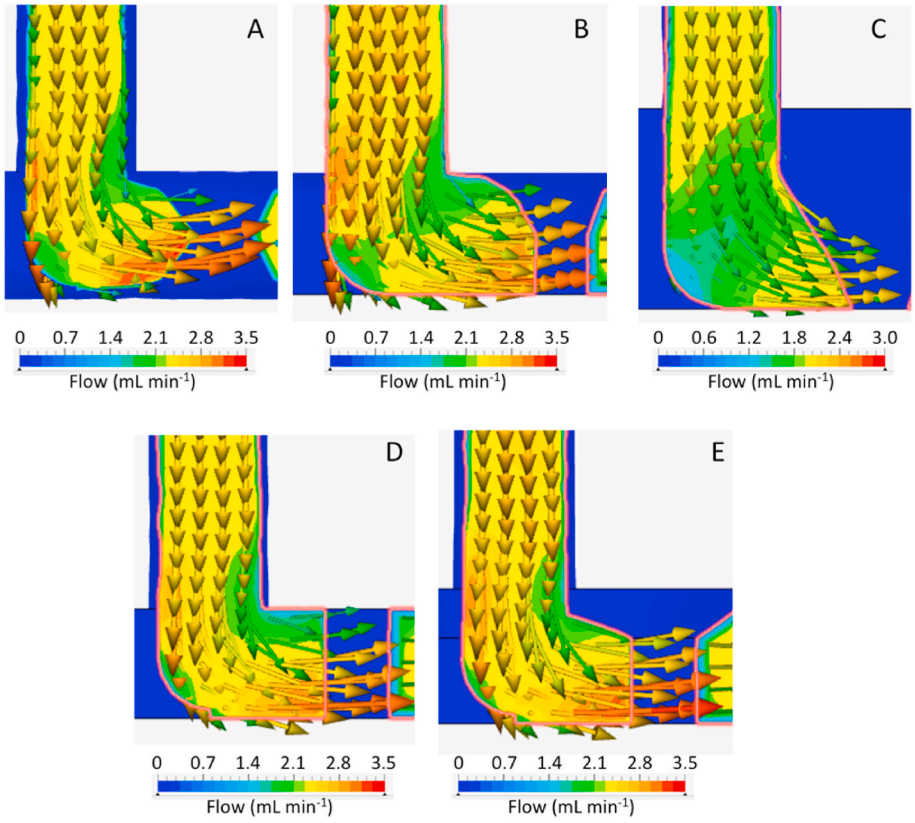

Fig. 5. Computer flow dynamics of the fluid motion (reagent + sample) at the inlet of the 3D-printed flow-cells with varied cross-sections: circular(A), semicircular (B), triangular (C), square (D) and 5-side polygon (E).

explained in the analytical method (see Experimental) is now proven unnecessary. In addition, the Y′-type confluence gives rise to partial deviation from the conventional laminar flow (Fig. S5C) expected in flow injection, which results in poorer precision values. Overall, the Y-type confluence demonstrated better analytical performance because it enables appropriate mixing of reagents by confluencing the streams in a radial rather than axial manner [41]. The analytical performance of the CL flow method incorporating the LFS-printed cell with 5-side polygon cross-section and Y-confluence was compared against that of two novel designs recently reported in the literature for the luminol–H_2O_2–Co(II) system, namely a Polyjet-printed radial flow-through cell [24] and a hollow bulb-shaped cell [42]. The LOD of our method is one decade better than those of the previous designs the applicability of which to real samples were only demonstrated for food commodities and pharmaceutical formulations at the μM level. One of the key features of our 3D-printed cell design is the perfect match of the detection zone of the cell with the PMT window.

Analytical applicability of the 3D-printed pentagonal cross-section flow-cell with the Y-type confluence was assessed for samples with a broad range of hydrogen peroxide concentrations and high matrix, such as seawater and human saliva. Samples were spiked at realistic concentrations, that is, nmol/L concentration levels for seawater [33], and μmol/L levels in saliva according to the findings by Chitra et al. [43] and the total ROS content in saliva reported by Roy et al. [44]. Matrix interfering effects onto the CL response were evaluated by comparing the external calibration in Milli-Q water with those obtained by matrix-match using undiluted synthetic seawater, and saliva at 1:400 and 1:1000 dilution factors. The sensitivity ratios of the external to seawater calibration and external to 1:1000 diluted saliva were 0.99 and 0.94, respectively, thus suggesting the lack of multiplicative matrix interferences. Hence, external calibration was selected for the recovery studies in saline waters and saliva. However, should the 1:400 or lower saliva dilution be needed the method of the standard addition had better use instead. The relative recoveries in seawater at the 116 nM and 232 nM levels, and saliva (diluted 1:1000) at the 0.23 and 0.46 mM levels were 96.7% and 82.7%, respectively, for seawater, and 101.0% and 102.9%, respectively, for saliva, with deviation in all cases $\leq$17% thus demonstrated the trueness and the reliability of the automatic CL method incorporating the 3D-printed pentagonal cell.

4. Conclusions

The unique opportunities of LFS for expedient one-step prototyping of microscale platforms that are not available by any other alternative subtractive fabrication approach (e.g. high precision milling) or more sophisticated printing technologies are in this work fully demonstrated with the printing of up to twenty CL flow cells with unrivalled cross-sectional geometry. By designing novel components of flow systems, *namely*, flow-through cells, tailored reactors and mixing zones with convoluted architectures, the applicability of the fourth generation of flow analysis, so-called 3D-μFIA [45] can be further expanded. Intricate geometries for the spirally-shaped CL cells (e.g., 5-side polygon cross-section), the reaction module, and the confluence zone just in front of the detection window have been herein proven superb for improving the analytical performance of flash CL methods (e.g., those based in luminol–H_2O_2–catalyst chemistry) against the conventional coiled tubing or methacrylate-milled spiral cells with circular cross-section by (i) enhancing forward-flow mixing of sample and reactants, and liquid velocities at the flow-cell entry as demonstrated by dynamic fluid simulations and (ii) improving the capture of elicited light by maximizing the solvent volume in the vicinity of the PMT window. Scaffolds as obtained by 3D printing also aided at reliably positioning the flow-cell onto the detection window. The incorporation of the 3D-printed modules in a hybrid flow system that enabled in-situ preparation of the composite CL reagent fostered unsupervised detection of hydrogen peroxide at concentration levels down to 12 nM as demanded in seawater analysis. Further work is underway to leverage the simplicity of 3D printing for fast prototyping of novel architectures to design CL cells adaptable to other chemistries, to glow-type CL reactions and to the detection of other reactive oxygen species (e.g. superoxide anion) in challenging matrices, such as those involving cell cultures.

Credit author statement

Llucia García-Moll: Investigation, Formal analysis, Writing – original draft, Visualization. Alexandra Sixto: Methodology, Investigation, Formal analysis, Validation, Writing – original draft. Enrique J. Carrasco-Correa: Conceptualization, Methodology, Formal analysis, Writing – review & editing, Supervision. Manuel Miró: Conceptualization, Methodology, Writing – review & editing, Supervision, Project administration, Funding acquisition.

Declaration of competing interest

The authors declare that they have no known competing financial interests or personal relationships that could have appeared to influence the work reported in this paper.

Data availability

The STL files of the CAD models (cells with distinct cross-section geometry and confluence types, and serpentine mixing coil) are available through ZENODO (DOI:10.5281/zenodo.7505100).

Acknowledgements

Manuel Miró and Enrique J. Carrasco-Correa acknowledge financial support from the Spanish State Research Agency (Agencia Estatal de Investigación, AEI/10.13039/501100011033), the Spanish Ministry of Science and Innovation (Ministerio de Ciencia e Innovación, MCIN) and the European Union (NextGenerationEU/PRTR) through projects PID2020-117686RB-C33 (AEI/MCIN) and TED2021-131303B–I00 (MCIN/AEI/NextGenerationEU/PRTR). Llucia Garcia-Moll is grateful to MCIN for funding an FPI-fellowship (PRE2021-100217). Enrique J. Carrasco-Correa also acknowledges the funding of the project PID2021-125459OB-I00 by the AEI (10.13039/501100011033) and the MCIN and the project CIGE/2021/117 funded by Generalitat Valenciana. Alexandra Sixto acknowledges the financial support from the UIB as a Visiting Professor, and to the Agencia Nacional de Investigación e Innovación (ANII, Uruguay) through project CSICI+D 2105.The authors are grateful to Dr. David J. Cocovi-Solberg for technical assistance and loan of CocoSoft software.

Appendix A. Supplementary data

Supplementary data to this article can be found online at https://doi.org/10.1016/j.talanta.2022.124211.

References

[1] P.N. Nesterenko, 3D printing in analytical chemistry: Current state and future, Pure Appl. Chem. 92 (2020) 1341–1355, https://doi.org/10.1515/pac-2020-0206.
[2] A. Ambrosi, A. Bonanni, How 3D printing can boost advances in analytical and bioanalytical chemistry, Microchim. Acta 188 (2021) 265, https://doi.org/10.1007/s00604-021-04901-2.
[3] V. Gupta, P.N. Nesterenko, B. Paull, 3D Printing in Chemical Sciences, The Royal Society of Chemistry, Cambridge, UK, 2019.
[4] J.S. Stefano, C. Kalinke, R.G. da Rocha, D.P. Rocha, V.A.O.P. da Silva, J.A. Bonacin, L. Angnes, E.M. Richter, B.C. Janegitz, R.A.A. Muñoz, Electrochemical (bio)sensors enabled by fused deposition modeling-based 3D printing: A guide to selecting designs, printing parameters, and post-treatment protocols, Anal. Chem. 94 (2022) 6417–6429, https://doi.org/10.1021/acs.analchem.1c05523.
[5] J. Muñoz, M. Pumera, 3D-printed biosensors for electrochemical and optical applications, TrAC, Trends Anal. Chem. 128 (2020), 115933, https://doi.org/10.1016/j.trac.2020.115933.

[6] F. Li, N.P. Macdonald, R.M. Guijt, M.C. Breadmore, Increasing the functionalities of 3D printed microchemical devices by single material, multimaterial, and print-pause-print 3D printing, Lab Chip 19 (2019) 35–49, https://doi.org/10.1039/c8lc00826d.

[7] D.J. Cocovi-Solberg, P.J. Worsfold, M. Miró, Opportunities for 3D printed millifluidic platforms incorporating on-line sample handling and separation, TrAC, Trends Anal. Chem. 108 (2018) 13–22, https://doi.org/10.1016/j.trac.2018.08.007.

[8] H.K. Balakrishnan, E.H. Doeven, A. Merenda, L.F. Dumée, R.M. Guijt, 3D printing for the integration of porous materials into miniaturised fluidic devices: a review, Anal. Chim. Acta 1185 (2021), 338796, https://doi.org/10.1016/j.aca.2021.338796.

[9] F. Li, M.R. Ceballos, S.K. Balavandy, J. Fan, M.M. Khataei, Y. Yamini, F. Maya, 3D Printing in analytical sample preparation, J. Separ. Sci. 43 (2020) 1854–1866, https://doi.org/10.1002/jssc.202000035.

[10] C.K. Su, Review of 3D-Printed functionalized devices for chemical and biochemical analysis, Anal. Chim. Acta 1158 (2021), 338348, https://doi.org/10.1016/j.aca.2021.338348.

[11] M. Belka, T. Bączek, Additive manufacturing and related technologies – the source of chemically active materials in separation science, TrAC, Trends Anal. Chem. 142 (2021), 116322, https://doi.org/10.1016/j.trac.2021.116322.

[12] U. Kalsoom, P.N. Nesterenko, B. Paull, Current and future impact of 3D printing on the separation sciences, TrAC, Trends Anal. Chem. 105 (2018) 492–502, https://doi.org/10.1016/j.trac.2018.06.006.

[13] E.J. Carrasco-Correa, E.F. Simó-Alfonso, J.M. Herrero-Martínez, M. Miró, The emerging role of 3D printing in the fabrication of detection systems, TrAC, Trends Anal. Chem. 136 (2021), 116177, https://doi.org/10.1016/j.trac.2020.116177.

[14] G.I.J. Salentijn, P.E. Oomen, M. Grajewski, E. Verpoorte, Fused deposition modeling 3D printing for (bio)analytical device fabrication: Procedures, materials, and applications, Anal. Chem. 89 (2017) 7053–7061, https://doi.org/10.1021/acs.analchem.7b00828.

[15] R.M. Cardoso, C. Kalinke, R.G. Rocha, P.L. Dos Santos, D.P. Rocha, P.R. Oliveira, B. C. Janegitz, J.A. Bonacin, E.M. Richter, R.A.A. Munoz, Additive-manufactured (3D-printed) electrochemical sensors: A critical review, Anal. Chim. Acta 1118 (2020) 73–91, https://doi.org/10.1016/j.aca.2020.03.028.

[16] Y. Liang, Q. Liu, S. Liu, X. Li, Y. Li, M. Zhang, One-step 3D printed flow cells using single transparent material for flow injection spectrophotometry, Talanta 201 (2019) 460–464, https://doi.org/10.1016/j.talanta.2019.04.009.

[17] M. Michalec, R. Koncki, L. Tymecki, Optoelectronic detectors for flow analysis systems manufactured by means of rapid prototyping technology, Talanta 198 (2019) 169–178, https://doi.org/10.1016/j.talanta.2019.01.092.

[18] F. Cecil, R.M. Guijt, A.D. Henderson, M. Macka, M.C. Breadmore, One step multi-material 3D printing for the fabrication of a photometric detector flow cell, Anal. Chim. Acta 1097 (2020) 127–134, https://doi.org/10.1016/j.aca.2019.10.075.

[19] J. Huang, Q. Qin, J. Wang, A review of stereolithography: Processes and systems, Processes 8 (2020) 1138, https://doi.org/10.3390/PR8091138.

[20] V. Cannizzaro, A.R. Bowie, A. Sax, E.P. Achterberg, P.J. Worsfold, Determination of cobalt and iron in estuarine and coastal waters using flow injection with chemiluminescence detection, Analyst 125 (2000) 51–57, https://doi.org/10.1039/a907651d.

[21] R.U. Shelley, B. Zachhuber, P.N. Sedwick, P.J. Worsfold, M.C. Lohan, Determination of total dissolved cobalt in UV-irradiated seawater using flow injection with chemiluminescence detection, Limnol Oceanogr. Methods 8 (2010) 352–362, https://doi.org/10.4319/lom.2010.8.352.

[22] J.M. Terry, E.M. Zammit, T. Slezak, N.W. Barnett, D.C. Olson, D.K. Wolcott, D. L. Edwards, P.S. Francis, Solution mixing and the emission of light in flow-cells for chemiluminescence detection, Analyst 136 (2011) 913–919, https://doi.org/10.1039/c0an00591f.

[23] K.B. Spilstead, J.J. Learey, E.H. Doeven, G.J. Barbante, S. Mohr, N.W. Barnett, J. M. Terry, R.M. Hall, P.S. Francis, 3D-printed and CNC milled flow-cells for chemiluminescence detection, Talanta 126 (2014) 110–115, https://doi.org/10.1016/j.talanta.2014.03.047.

[24] V. Gupta, P. Mahbub, P.N. Nesterenko, B. Paull, A new 3D printed radial flow-cell for chemiluminescence detection: Application in ion chromatographic determination of hydrogen peroxide in urine and coffee extracts, Anal. Chim. Acta 1005 (2018) 81–92, https://doi.org/10.1016/j.aca.2017.12.039.

[25] R.G. Wetzel, G.E. Likens, Limnological Analyses, third ed., Springer, New York, 2000 https://doi.org/10.1007/978-1-4757-3250-4.

[26] D.J. Cocovi-Solberg, M. Miró, CocoSoft: Educational software for automation in the analytical chemistry laboratory, Anal. Bioanal. Chem. 407 (2015) 6227–6233, https://doi.org/10.1007/s00216-015-8834-8.

[27] F.A.S. Vaz, L.N.O. Neves, R. Marques, R.T. Sato, M.A.L. Oliveira, Chromophoreasy, an excel-based program for detection and integration of peaks from chromatographic and electromigration techniques, J. Braz. Chem. Soc. 27 (2016) 1899–1911, https://doi.org/10.5935/0103-5053.20160076.

[28] D.J. Cocovi-Solberg, M. Rosende, M. Michalec, M. Miró, 3D Printing: The second dawn of Lab-on-Valve fluidic platforms for automatic (bio)chemical assays, Anal. Chem. 91 (2019) 1140–1149, https://doi.org/10.1021/acs.analchem.8b04900.

[29] P.J. Worsfold, R. Clough, M.C. Lohan, P. Monbet, P.S. Ellis, C.R. Quétel, G.H. Floor, I.D. McKelvie, Flow injection analysis as a tool for enhancing oceanographic nutrient measurements-A review, Anal. Chim. Acta 803 (2013) 15–40, https://doi.org/10.1016/j.aca.2013.06.015.

[30] A. Milne, M.S. Davey, P.J. Worsfold, E.P. Achterberg, A.R. Taylor, Real-time detection of reactive oxygen species generation by marine phytoplankton using flow injection-chemiluminescence, Limnol Oceanogr. Methods 7 (2009) 706–715, https://doi.org/10.4319/lom.2009.7.706.

[31] J.A. Murillo-Pulgarín, L.F. García-Bermejo, A. Carrasquero-Durán, A fast and simple FIA-chemiluminescence method for the evaluation of Roselle flowers as scavenger of the free radicals generated by UV irradiated antibiotics, J. Pharm. Biomed. Anal. 164 (2019) 630–635, https://doi.org/10.1016/j.jpba.2018.11.004.

[32] M. Manera, M. Miró, J.M. Estela, V. Cerdà, A multisyringe flow injection system with immobilized glucose oxidase based on homogeneous chemiluminescence detection, Anal. Chim. Acta 508 (2004) 23–30, https://doi.org/10.1016/j.aca.2003.11.050.

[33] D. Price, P.J. Worsfold, R. Fauzi, C. Mantoura, Determination of hydrogen peroxide in sea water by flow-injection analysis with chemiluminescence detection, Anal. Chim. Acta 298 (1994) 121–128, https://doi.org/10.1016/0003-2670(94)90050-7.

[34] S. Uchida, Y. Satoh, N. Yamashiro, T. Satoh, Determination of hydrogen peroxide in water by chemiluminescence detection, (II) theoretical analysis of luminol chemiluminescence processes, J. Nucl. Sci. Technol. 41 (2004) 898–906, https://doi.org/10.1080/18811248.2004.9715562.

[35] S. Garg, A.L. Rose, T.D. Waite, Production of reactive oxygen species on photolysis of dilute aqueous quinone solutions, Photochem. Photobiol. 83 (2007) 904–913, https://doi.org/10.1111/j.1751-1097.2007.00075.x.

[36] W.J. Cooper, J.K. Moegling, R.J. Kieber, J.J.A. Kiddle, A chemiluminescence method for the analysis of H_2O_2 in natural waters, Mar. Chem. 70 (2000) 191–200, https://doi.org/10.1016/S0304-4203(00)00025-6.

[37] D.W. King, W.J. Cooper, S.A. Rusak, B.M. Peake, J.J. Kiddle, D.W. O'Sullivan, M. L. Melamed, C.R. Morgan, S.M. Theberge, Flow injection analysis of H_2O_2 in natural waters using acridinium ester chemiluminescence: Method development and optimization using a kinetic model, Anal. Chem. 79 (2007) 4169–4176, https://doi.org/10.1021/ac062228w.

[38] A. Townshend, R.A. Wheatley, Oxidative chemiluminescence assay of 2,4-dinitrophenylhydrazine, Analyst 123 (1998) 1041–1046, https://doi.org/10.1039/a708350e.

[39] D.L. Massart, B.G.M. Vandeginste, L.M.C. Buydens, S. De Jong, P.J. Lewi, J. Smeyers-Verbeke, Handbook of Chemometrics and Qualimetrics: Part A, Vol. 20A, Elsevier, The Netherlands, 1998.

[40] M. Manera, M. Miró, M.F. Ribeiro, J.M. Estela, V. Cerdà, J.J. Santos, J.L.F.C. Lima, Rapid chemiluminometric determination of gabapentin in pharmaceutical formulations exploiting pulsed-flow analysis, Luminescence 24 (2009) 10–14, https://doi.org/10.1002/bio.1055.

[41] J. Ruzicka, E.H. Hansen, Flow Injection Analysis, second ed., John Wiley, New York, 1988, pp. 152–154.

[42] E.G. Brandão, S.R.W. Perdigão, B.F. Reis, A new flow cell design for chemiluminescence detection using an improved signal transduction network. Determination of hydrogen peroxide in pharmaceuticals, Microchem. J. 171 (2021), 106789, https://doi.org/10.1016/j.microc.2021.106789.

[43] S. Chitra, M. Balasubramaniam, J. Hazra, Effect of α-tocopherol on salivary reactive oxygen species and trace elements in oral submucous fibrosis, Ann. Clin. Biochem. 49 (2012) 262–265, https://doi.org/10.1258/acb.2011.011050.

[44] J. Roy, N. Manjunath, K. Bhat, A. George, F. Nishana, L. Mathew, Estimation of salivary glycoconjugates and salivary ros levels in chronic periodontitis: A clinico-biochemical study, Int. J. Res. Med. Sci. 5 (2017) 3578–3583, https://doi.org/10.18203/2320-6012.ijrms20173566.

[45] H. Wang, D.J. Cocovi-Solberg, B. Hu, M. Miró, 3D-Printed microflow injection analysis platform for online magnetic nanoparticle sorptive extraction of antimicrobials in biological specimens as a front end to liquid chromatographic assays, Anal. Chem. 89 (2017) 12541–12549, https://doi.org/10.1021/acs.analchem.7b03767.